ChemPhysChem

Research Article
doi.org/10.1002/cphc.202200867

Chemistry Europe
European Chemical Societies Publishing

www.chemphyschem.org

Elucidating the N–N and C–N Bond-breaking Mechanism in the Photoinduced Formation of Nitrile Imine

Cristian Guerra,*[a, b] Leandro Ayarde-Henríquez,*[a, c] Yeray A. Rodríguez-Núñez,[d] Adolfo Ensuncho,[b] and Eduardo Chamorro*[a]

In this study, we revealed the significance of chemical bonding for the photochemically induced mechanism of 2-phenyl tetrazole derivatives generating nitrile imines. The correlated electron localization function shows that the formation of imine nitrile involves two key bond events: (i) the heterolytic C–N breakage taking place in the T_1 state and (ii) the homolytic N–N rupture occurring in the T_2 excited state. In particular, a cation-radical specie results from the C–N cleavage, whereas the N–N rupture creates a biradical resonant form of imine nitrile. Additionally, we noticed that the substantial pair delocalization of the C–C-N bonded structure could play a significant role in the conversion of the biradical imine nitrile into both the propargylic and allenic forms via the $T_1 \rightarrow S_0$ deactivation.

Introduction

Tetrazole-ene cycloaddition is an important reaction route that has been recently revisited.[1–5] This process requires a previous photochemical generation of the nitrile imine (NIm) compounds for its subsequent cycloaddition in the ground state.[1] The high reactivity of NIm species includes different valence structures generated mainly through N_2 elimination from 2,5-tetrazoles.[6–9] The photochemical reaction mechanism of NIm production is the subject of ongoing research through experimental and theoretical methods.[3,6,7] In this context, Flesh and Vöhringer combined the femtosecond UV/IR spectroscopy with TD-DFT calculations of the 2,5-diphenyl tetrazole (Dtz) system.[6] This study showed that the N_2 extrusion occurs in multiple adiabatic transitions from the S_1 excited state toward triplet states. Interestingly, the ultrafast dynamics which explain the NIm formation strongly suggest that the key bonding process resulting in the N–C and N–N bond cleavage takes place on the triplet potential energy surfaces.[5–7] Moreover, the real-time IR analysis concerning the normal modes of Dtz enables identifying the vibrations of resonance structures responsible for the light-induced mechanism of cycloelimination of N_2.[10–14] This fact is particularly relevant because changes in C–N and N–N stretching modes along the reaction process allow us to picture how the NIm species are formed.[6] Moreover, a deeper understanding of this (and others) chemical reaction can be gained using spectroscopic data analysis. Nevertheless, in the case of 2,5-tetrazole photochemistry, some fundamental mechanistic aspects concerning to NIm formation mechanism are elusive even for the high-resolution experimental methods. In such a context, consider the photochemical route proposed by Barner-Kowollik and coworkers for the NIm formation mechanism shown in Scheme 1.[5] The π–π^* transition ($S_0 \rightarrow S_1$) leads to the S_1-excited state, and subsequently, the excited tetrazole accesses the T_n excited state via intersystem crossing (ISC). The evolution of such a reaction system decaying non-adiabatically from the T_n state results in the N_2 elimination, whereas the NI formation occurs through the T_1/S_0 conical intersection.[6,7] It should be stressed that this brief description of 2,5-tetrazole photolysis leaves undiscovered the bonding nature of different excited-state reaction stages leading to both photoproducts.

In particular, the N–N and C–N bond breaking are the main bonding events driving the NIm formation. Consequently, a deeper understanding of such a mechanism should be strictly bound up with electronic rearrangements resulting in the cleavage of these bonds. The absence of investigations focused on explaining how the N–N and N–C bonds break along a path on the T_n surface drives us to conduct a theoretical study of the NIm generation mechanism using multiconfigurational *ab initio* and quantum chemical topology methods. Herein, we sought to support the remarkable recent research by Flesh and Vöhringer focused on elucidat-

[a] Dr. C. Guerra, Dr. L. Ayarde-Henríquez, Prof. Dr. E. Chamorro
Universidad Andrés Bello, Facultad de Ciencias Exactas, Departamento de Ciencias Químicas, Centro de Química Teórica & Computacional (CQT&C), Avenida República 275, 8370146, Santiago de Chile. Chile
E-mail: c.guerramadera@uandresbello.edu
Leandro.Ayarde@tcd.ie
echamorro@unab.cl
[b] Dr. C. Guerra, Prof. A. Ensuncho
Universidad de Córdoba, Facultad de Ciencias Básicas, Grupo de Química Computacional. Carrera 6 No. 77-305 Montería-Córdoba, Colombia
E-mail: aensuncho@correo.unicordoba.edu.co
[c] Dr. L. Ayarde-Henríquez
Trinity College Dublin, The University of Dublin, School of Physics, College Green Dublin 2, Ireland
[d] Dr. Y. A. Rodríguez-Núñez
Universidad Andrés Bello, Facultad de Ciencias Exactas, Departamento de Ciencias Químicas, Avenida República 275, 8370146, Santiago de Chile, Chile
E-mail: yeray.rodriguez@unab.cl

Supporting information for this article is available on the WWW under https://doi.org/10.1002/cphc.202200867

Research Article
doi.org/10.1002/cphc.202200867

Chemistry Europe
European Chemical Societies Publishing

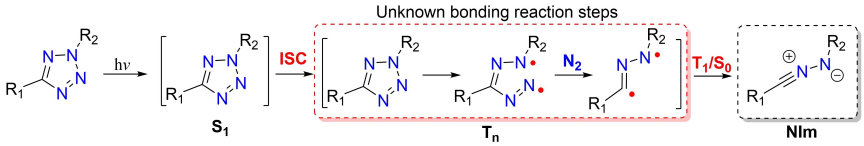

Scheme 1. Photochemical generation route of nitrile imine from 2,5- substituted tetrazole. The reaction steps highlighted in red constitute the focus of this work In order to preserve the high resolution of pictures, please take them from the PDF files provided.

ing such a molecular mechanism. In analogy with the time-resolved methods employed in ref [7], we analyzed the evolution of the electronic structure of the tetrazole ring along the intrinsic reaction coordinated (IRC)[15,16] connecting the most relevant energy stationary points implied in the NIm generation.[6,7] Our representation of electron reorganizations is based on the electron localization function (ELF ≡ η(r)) analysis.[17–20] ELF constitutes a measure of electron pairs localization derived from the same-spin-pair conditional probability.[18] This function exhibits pair localization maxima in regions where it is highly probable to find a second electron near the reference one (located at a given point), having both fermions parallel spins. These regions are associated mainly with bonds and lone pairs, concepts inherent to the VSEPR theory.[21,22] More specifically, mathematical objects such as basins and critical points derived from ELF topology analysis, constitute universal chemical bond descriptors successfully applied to describe the electronic structure of crystals and molecular systems.[23–25] In our abiding interest of giving a closer look at the NIm formation mechanism in the excited state, we monitored the changes in the ELF topology along the reaction coordinates featuring the N_2 extrusion and the NI formation in T_2, T_1, and S_0 states for the 2-phenyl tetrazole system. This methodology, the so-called bonding evolution theory (BET), provides critical information about the electron pairing fluxes, allowing thus to describe the reaction through a sequence of different Lewis-like structures.[22,26–31] Therefore, our goal is to enrich the current understanding of the molecular mechanism driving the nitrile imine generation, complementing the photodynamic studies beforehand.

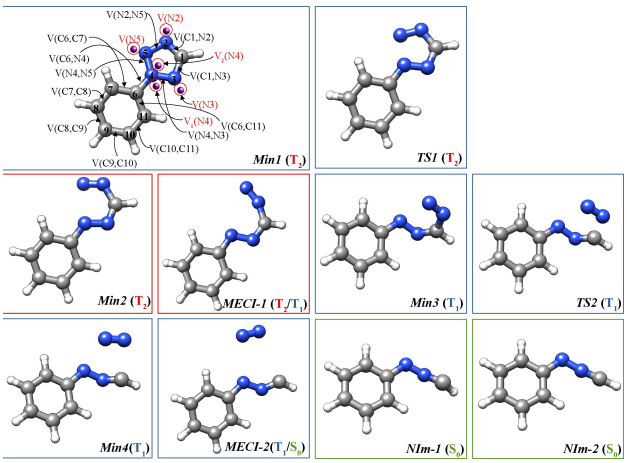

Figure 1. Energy stationary points optimized at CASSCF(10,8)/6-31g(d) level for the photochemically induced NI formation from the 2-phenyl tetrazole ring. ELF basins are shown for the Min1 structure. V(X,Y) basins represent bonds and V_i(X) represents lone pair regions. In order to preserve the high resolution of pictures, please take them from the PDF files provided.

Results and Discussion

Figure 1 shows the energy stationary points calculated using the complete active space self-consistent (CASSCF) method. We chose the IRC for analyzing the NIm formation over the PES relaxed method.

Considering the results provided by Barner-Kowollik and coworkers,[5] the T_2, T_1, and S_0 electronic states constitute our main reaction paths, allowing us to give the following mechanistic description: (*i*) TS1 transition state connects intermediates *Min1* and *Min2* formed in the T_2 state. (*ii*) The *Min1→MECI-1* reaction path indicates the deactivation of the reaction center after the systems moved from the T_2 to T_1 state via T_2/T_1 non-adiabatic crossing. (*iii*) The *Min3→Min4* involving the TS2 transition state in the T_1 state, (*iv*) The *MECI-2→NIm-1* path representing the deactivation of reaction system from the *MECI-2* (T_1/S_0) conical intersection towards the nitrile imine; namely, *NIm-1* in the ground state, (*v*) The *Nim-1→NIm-2* connecting both *NIm-1* and *NIm-2* resonant structures. By considering the *Min1* structure, we have included the molecular graph obtained from ELF topological analysis for *Min1*. This graph shows the ELF-maxima associated with high electron-pair localization regions or basins.[19,32] Monosynaptic basins labeled as V_i(X) represent non-bonding regions such as lone pairs or radical centers associated with the nucleus X, whereas V(X,Y) indicates a bond interaction between nuclei X and Y.

The nature of bonds, lone pairs, or radical centers is then given by the average number of electrons, $N_{V(X,Y)}$, measured over these regions. For instance, the V(N,C) and V(N,N) basins represent the N–C and N–N bonds of the tetrazole ring for the *Min1* structure, whereas V_i(N) are directly associated with lone pairs and non-bonding regions inherent to the nitrogen valence shell. The photochemistry of Dtz leading to the *Min1* formation implies the passage of the former from the S_n excited state towards the intersystem crossing. However, due to the similarity between Dtz and *Min1* geometries, we have focused on the reaction paths leading to both N–N and C–N bond cleavage. Regardless that along the *Min→Min1* transformation, valence basins (bond and lone pairs) do not

disappear or appear; we described chemical bonding changes by means of the ELF topology analysis because relevant modifications in the pairing density occur. The (*i*)–(*iv*) paths entail sudden changes in the ELF topology describing the bonding features of the reaction system. Such changes can be associated with key chemical bonding events according to the BET approach.

The energy barrier of the *Min1*→*Min2* process is about 16.80 kcal mol^{-1}, as shown in Figure 2. This path was plotted as a function of the N4–N5 distance, wherein the dashed vertical lines indicate significant bonding events taking place along the reaction coordinate. At P_1, the V_2(N4) disappears, suggesting the vanishing of one of the N4 non-bonding regions. The pairing density depleted from the N4 zone redistributes towards the N4–C6 bond, which acquires a polarized bond character since $N_{V(N4,C6)}$ increases from 2.22 to 2.67***e***. The disappearance of the N4 non-bonding center leaves N4 only with the V_1(N4) radical-like center ($N_{V1(N4)}$ = 1.1***e***). This electronic rearrangement occurs before the system reaches the TS1 transition state (d_{N4-N5} = 1.57 Å), implying an energetic change of 12.61 kcal mol^{-1} along the *Min1*→P_1 process.

At TS1, the N4–N5 bond breaks (d_{N4-N5} = 2.23 Å), and the pairing density flows and accumulates merely on the N4 atom, forming the new V_3(N4) basin with 1.8***e***. Moreover, the $N_{V(C1,N3)}$ and $N_{V(C1,N3)}$ populations increase up to 2.5***e***, leading to a high delocalization of the density over the C1–N2 and C1–N3 bonds. The V_1(N4) monosynaptic basin disappears at the P_2 configuration when the system moves from TS1 to *Min2*. The pairing density depletes such a region and transfers mainly towards V_3(N4) lone pair, releasing the reacting system about 5.19 kcal mol^{-1}. The high delocalization characterizing both the C1–N2 and C1–N3 bonds disappears at P_2 because the population of C1–N2 decreases up to 2.0***e***, whereas the C1–N3 population increases to 3.1***e***. Interestingly, the electronic population of the N5 non-bonding center increases from 3.24 to 3.70***e*** once the *Min2* emerges. This rearrangement marks the onset of two lone pairs formation near the N5 atom. However, the accumulation of pairing density on N5 does not result from the N4–N5 cleavage; it is a consequence of electron fluxes from the N4 to N5 valence shell, occurring on the downhill energy direction of the reaction path. At *Min2*, the number of electrons in the N4 and N5 valence shells are as high as 6.16 and 6.86***e*** on average, respectively. In the case of N5, it could be related to a positive charge, whereas N4 has a radical behavior. Thus, the nature of the *Min2* intermediate could be essentially a radical-like cation resulting from the heterolytic rupture of N4–N5. These electronic rearrangements have previously been reported in the literature for thermal- and light-induced reactions,[33–36] wherein heterolytic cleavages generate radical cation species. Based on BET analysis, our results point out that the triplet spin multiplicity of tetrazole moiety might promote the formation of transient radical-cation species via N–N heterolytic fragmentation. From *Min2*, the reaction system can decay to the T_1 surface through the *MECI-1* conical intersection, reaching *Min3*. The *Min2*→*MECI-1* process implies the full ring opening of tetrazole (d_{N4-N5} = 3.08 Å), flowing the pairing density from the N2 valence shell to the C1–N3 bond, as suggested by the electronic populations reported in Table 1.

Once the ring opens, tetrazole reaches the T_1 state and the N5 lone pairs are fully formed since V(N5) basins split into V_1(N5) and V_2(N5), with $N_{V1(N5)}$ = 1.89***e*** and $N_{V2(N5)}$ = 1.86***e***. Nonetheless, the N5 valence shell still integrates about 6.38***e***. The positive character of N4 could be observed in the T_1 state. The electron rearrangements associated with N5 and N2 valence shells are energetically favorable since both *Min2*→*MECI-1* and *MECI-1*→*Min3* are exothermic processes. The first one results from the N4–N5 elongation; in contrast, the second is due to the out-of-plane rotation of the N2–C1–N3 fragment. Detailed geometric data for the stationary points can be found in the supporting information file.

The breaking of the C1–N2 bond occurs along the *Min3*→*Min4* process via the TS2 transition state (see Figure 3). However, before TS2 is reached, one lone pair of N5 annihilates. This change occurs at the P_4 configuration involving about 1.43 kcal mol^{-1}, wherein both V_1(N5) and V_2(N5) merge, resulting in a single lone pair region, V(N5), with a population of 3.58***e***. Once the system reaches the TS2

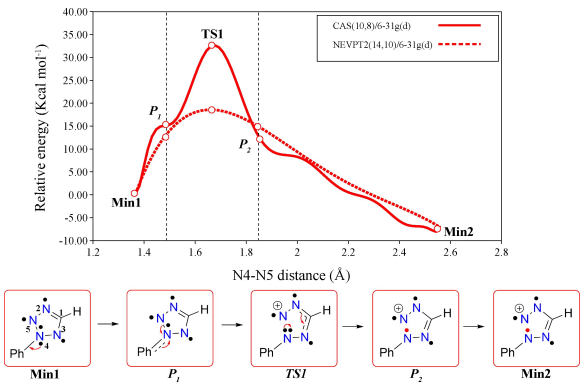

Figure 2. Variation of the relative energy ΔE(=E_{Min1}-E_i) along the N4–N5 distance associated with the *Min1*→*Min2* evolution in the T2 excited state. Red solid curve indicates E values computed at the CAS(10,8)/6-31g(d) level, whereas the dotted one shows ΔE values using the NEVPT2 correction and the expansion of the active space to CAS(14,10). Vertical lines show the N4–N5 value corresponding to each bonding configuration (P_n). The Lewis-like representation of each P_n configuration depicts the electron pair distribution along the chemical transformation within the BET approach. Red and filled black dots indicate radical centers and lone pairs, respectively. In order to preserve the high resolution of pictures, please take them from the PDF files provided.

Table 1. Electronic populations for V(Ci) and V(Ci,Cj) valence basins associated with relevant stationary points in the 2-phenyl tetrazole photochemistry.

	V(C1,N3)	V(C1,N2)	V(N3,N4)	V(N2,N5)	V(N2)
Min2 (T_2)	3.11	1.82	1.77	2.44	2.78
MEC1-1(T_2/T_1)	3.11	2.21	1.65	2.44	2.25
Min3 (T_1)	3.23	1.88	1.74	2.81	2.49
	V(N3)	V(N5)	V_3(N4)	V_1(N5)	V_2(N5)
Min2 (T_2)	2.70	3.71	2.80	–	–
MEC1-1(T_2/T_1)	2.75	3.85	2.93	–	–
Min3 (T_1)	2.54	–	2.94	1.89	1.68

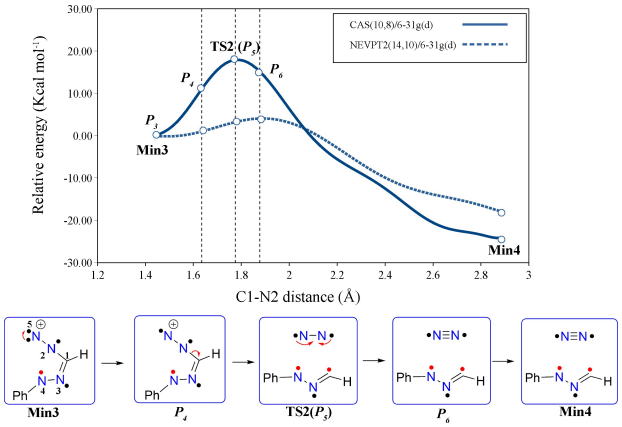

Figure 3. Variation of the relative energy ΔE(= E_{Min3}-E_i) along the C1–N2 distance associated with the *Min3*→*Min4* evolution in the T1 excited state. Red solid curve indicates E values computed at the CAS(10,8)/6-31g(d) level, whereas the dotted one shows ΔE values using the NEVPT2 correction and the expansion of the active space to CAS(14,10). Vertical lines depict the N4–N5 value corresponding to each bonding configuration (P_n). The Lewis-like representation of each P_n configuration shows the electron pair distribution along the chemical transformation within the BET approach. Red and filled black dots indicate radical centers and lone pairs, respectively In order to preserve the high resolution of pictures, please take them from the PDF files provided.

state (P_5 configuration), the C1–N2 bond breaks and the pairing density accumulates only on the C1 atom, which originates the V(C1) basin with $N_{V1(N4)} = 1.1\boldsymbol{e}$. Thus, the C1 center acquires a radical-like character since the number of electrons of the C1 valence shell is 6.63***e*** at TS2. It should be noted that at this point, the N4 valence shell electrons are 6.99***e***, indicating a strong radical behavior.

Noteworthy, the C1–N2 breaking results in the N_2 extrusion occurring on the T_1 surface ($d_{C1-N2} = 1.68$ Å), demanding 5.97 kcal mol^{-1}. Departing from TS2 and moving towards *Min4*, the P_5 configuration concerns the full formation of the N_2 diatomic molecule. The N–N bond, ($N_{V(N5,N2)} =$ 3.7***e***), forms due to the electron pairing rearrangements encompassing the depletion of both N5 and N2 non-bonding regions. The remaining nitrile imine fragment associated with the *Min4* corresponds to a biradical structure. This asseveration is supported by the polar features of C1 and N4 and the fact that the N3 nonbonding center corresponds to the lone pair region, as indicated by the electronic populations presented in Table 2. Furthermore, both N4 and C1 valence electrons are, on average, 7.0***e***, which certainly constitutes another factor indicating a biradical character for the NIm specie in the T_1 excited state. This finding is according to the mechanistic discussion of Flesh and Vöhringer. Particularly, our BET analysis suggests that such species are generated via homolytic fragmentation of the N–C bond in a state with triplet spin multiplicity.

The *Min4* structure deactivates to the ground state via *MECI-2* conical intersection since it is energetically unstable mainly due to the distorted C1–N3–N4 angle (∠C1–N3–N4 = 130°). Our calculations point out that both allenic and propargylic forms of NIm (*NmI-1* and *NmI-2*, respectively) can be obtained from the *MECI-2* funnel. Figure 4 depicts the relaxation path leading to the *NmI-1* formation via *MECI-2*, wherein the C1–N3–N4 vary from a strongly distorted geometry to a quasi-planar array. This change facilitates the C1–N3 bond formation at the P_7 configuration. The electron population of the N3 lone pair transfers towards the C1–N3 ($N_{V(C1,N3)} = 4.50\boldsymbol{e}$), acquiring a semi-triple bond character. Furthermore, both electronic rearrangements involve −5.80 and −6.11 kcal mol^{-1}, respectively.

Both $N_{V(N4)}$ and $N_{V(C1)}$ populations increase to 3.60 and 1.60***e***, respectively, indicating the partial formation of two lone pairs near the N4 atom and the appearance of one lone pair in the locality of C1. In addition, the number of valence shell electrons of the N4 and C1 atoms sums up to 8***e***. This behavior suggests the disappearance of radical-like character (observed in the T_n states) once the NIm decays to the ground state. The bonding structure of *Min4* resembles an allenic form since the C1–N3 bonds have an electron population of 4.5***e***, indicating a highly delocalized double bond. Notably, the electron population of the N3–N4 bond is 2.29***e*** suggesting a weak polarized bond character. Nevertheless, it should be remarked that the NIm species are quite

Table 2. Valence electronic populations for V(Ci) and V(Ci,Cj) basins associated with relevant stationary points of 2-phenyl tetrazole photochemistry.

	V(C1,N3)	V(C1)	V(N3,N4)	V(N3)	V3(N4)
Min4	3.13	1.41	1.75	2.29	2.94
TS2	3.45	1.10	1.75	2.34	2.94
Min3	3.23	–	1.75	2.53	2.93
MECI-2	3.03	1.35	1.77	2.29	2.92
NIm-1	4.50	1.63	2.29	–	3.60
NIm-2	5.02	0.24	2.19	–	3.40

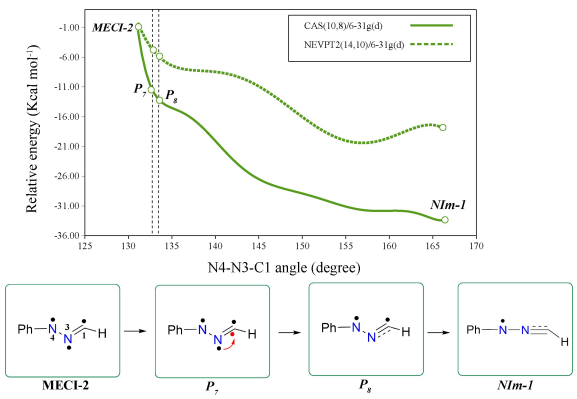

Figure 4. Variation of the relative energy ΔE(= E_{MECI-2}-E_i) along the N4–N3–C1 angle associated with the system evolution from *MECI-2* to *NIm-1* in the ground state. Red solid curve indicates E values computed at the CAS(10,8)/6-31g(d) level, whereas the dotted one shows ΔE values using the NEVPT2 correction and the expansion of the active space to CAS(14,10). Vertical lines show the N4–N3–C1 value corresponding to each bonding configuration (P_n). The Lewis-like representation of each P_n configuration depicts the electron pair distribution along the chemical transformation within the BET approach. Red and filled black dots indicate radical centers and lone pairs, respectively. In order to preserve the high resolution of pictures, please take them from the PDF files provided.

reactive; therefore, this feature is reflected in its bonding electronic structure. Figure 5 shows the delocalization indexes calculated for *NIm-1* between the N3–N4 bond and the C1 and N4 lone pairs, including also the C1–N3 bond. In allenic and propargylic forms, a high electron population delocalizes from the C1–N3 bond and N4 lone pairs towards the N3–N4 bond (~1.71***e***). This trend persists even for substituted imines. Thus, the high electron delocalization of NIm could be strictly related to the coexistence of a broad variety of resonant structures.

The formation of propargylic species from allenic occurs spontaneously (ΔG =-19.92 kcal mol^{-1}) involving a relatively low energetic barrier of 8.01 kcal mol^{-1}, as shown in Figure 6. The variation in the N3–C1–H angle (θ) from 131° to 180° induces the migration of pairing density from C1 lone pairs to C1–N3 ($N_{V(C1,N3)}$ = 5.02***e***), forming thus a weak triple bond between these atoms. Interestingly, the C1 non-bonding density does not disappear completely, remaining two non-bonding centers

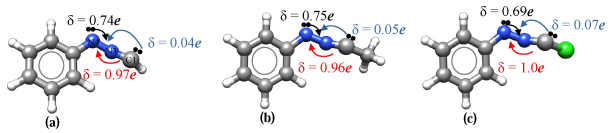

Figure 5. Electron delocalization indexes for the *NIm-1* structures computed between the N4-N3 bond and three regions, namely, both the N4 and C1 lone pairs and the N3–C1 bond (a panel). The methyl and chloro substituted nitrile imine are also depicted (b and c panels). Arrows indicate the delocalization of electrons towards N4–N3 region. In order to preserve the high resolution of pictures, please take them from the PDF files provided.

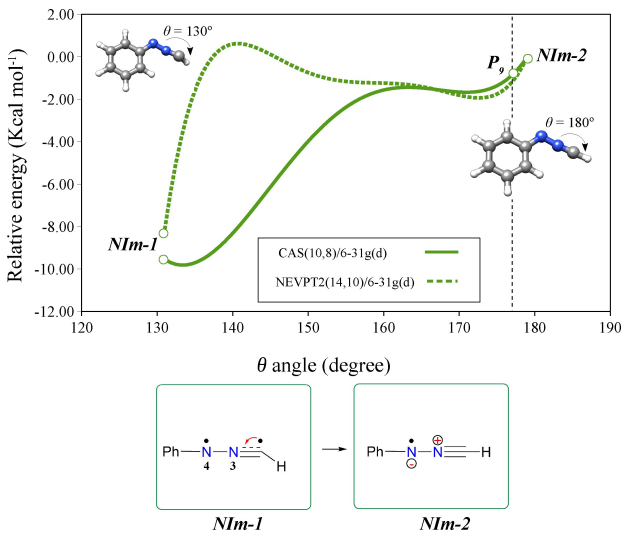

Figure 6. Variation of the relative energy ΔE(=E_{NIm-1}-E_i) as a function of the N3–C1–H angle, encompassing the evolution from *NIm-1* to *NIm-2* in the ground state. Red solid curve indicates E values computed at CAS(10,8)/6-31 g(d) level, whereas the dotted one shows ΔE values using the NEVPT2 correction and the expansion of the active space to CAS(14,10). Vertical lines show the N3–C1–H value corresponding to each bonding configuration (P_n). The Lewis-like representation of each P_n configuration depicts the electron pair distribution along the chemical transformation within the BET approach. Red and filled black dots indicate radical centers and lone pairs, respectively. In order to preserve the high resolution of pictures, please take them from the PDF files provided.

V(C1) with 0.24***e***. Thus, the migration of lone pair electrons from the C1 atom is mainly accountable for the appearance of the C1–N3 triple bond in the propargylic form starting from the allenic specie in the ground state.

Figure 7 summarizes our findings concerning the elucidation of critical bonding events featuring the photochemical-induced nitrile imine formation. Once the S_1-excited tetrazole reaches the higher triplet state (T_2, in our case), the N–N may break, giving a radical cation intermediate through a heterolytic process demanding 16.08 kcal mol^{-1}. The T_2/T_1 crossing is favored by the full ring opening of radical tetrazole due to electronic rearrangements linked to the N4 valence shell. The radical character is preserved upon deactivation towards the T_1 state, in which the C–N bond homolytically breaks, yielding the nitrile imine diradical form. The N_2 extrusion occurs essentially from both the N–N and C–N cleavage processes over the T_2 and T_1 energy surfaces. Specifically, we observed that at the T_1/S_0 conical intersection, the distorted imine nitrile and N_2 fragments are formed already.

This diradical nitrile imine form deactivates to the ground state mainly because the CNN-angle straightens. We found that the allenic resonant form primarily produces through the T_1/S_0 conical intersection, disappearing the radical character of imine in the ground state. The conversion of allenic form into propargylic is a spontaneous process involving a low energy barrier, favoring the highly delocalized C–N and N–N bonds the switching between resonant structures. These findings contribute to a better understanding of the intricate photochemical processes that turn tetrazoles into nitrile imines. Certainly, the pivotal experimental investigations made by Flesh and Vöhringer constitute a breakthrough in such a field. Our results are in good agreement with these experimental observations and allow us to give a closer look at the N–N and C–N bond formation/breaking process concerning the photochemistry of tetrazoles. Regardless that a simple mechanistic interpretation in terms of Lewis-type structures is proposed, we are convinced that a complete elucidation of this complex mechanism requires distinct methodologies, such as the non-adiabatic quantum dynamics approach.

Computational Methodology

The identification of different resonant structures of nitrile imine demands a multiconfigurational treatment of electronic structures. Ab-initio calculations concerning 2-phenyl tetrazole were carried out at CASSCF(10,8)/6-31g(d) level to refine the TD-DFT calculations performed by Flesh and Vöhringer. Aiming to yield reliable energy barriers, we performed an enlargement of the active space from CAS(10,8) to CAS(14,10). Also, second order multireference perturbation theory calculations based on the NEVPT2 formalism were carried out. IRC calculations are based on the vibrational frequencies of the transition states and minimum energy points conical intersection points (*TS1*, *TS2*, *MECI-1*, and *MECI-2*). Herein, the minimum energy conical intersection points were optimized using the MC-SCF lagran-

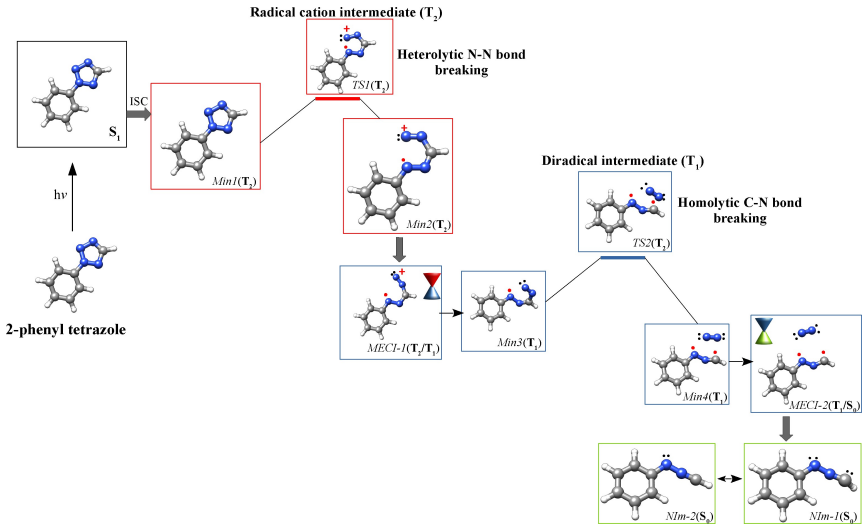

Figure 7. Photochemical route for the NIm formation, including key bonding processes unraveled from the bonding evolution theory. In order to preserve the high resolution of pictures, please take them from the PDF files provided.

gian method avaiable in Gaussian09 program.In this work, we used the correlated version of the ELF derived by *Matito et al.*[17,37] and linked to the Topmod package.[38] Thus, the second-order density matrix for ELF was computed from both CI and CASSCF orbital coefficients using the DMN program.[17] ELF topological analysis was carried out using both Topmod and Multiwfn 3.8 software.[39] Note that ELF calculations using the wave functions generated from CAS(14,10)/6-31g(d) and NEVPT2(14,10)/6-31g(d) are indeed close to those initially obtained by the CAS(10,8)/6-31g(d) method. Thus, we have decided to use the latter to discuss chemical bonding implications of the photo-induced formation of nitrile imine mechanism. This data is available from the authors upon request.

Supporting Information Summary

A detailed data concerning the geometry of stationary points is available in the supporting information file, as well as the following additional references.[40–43]

Acknowledgements

The authors thank UNAB and the ANID/CONICYT Ph.D. scholarships awarded to C. Guerra and L. Ayarde-Henríquez, respectively. Also, we are indebted to the Fondo Nacional de Ciencia y Tecnología (FONDECYT-ANID, Chile) for the continuous financial and academic support provided through Projects No. 1181582, 1221383, and 1231018. Open Access funding provided by IReL.

Conflict of Interest

The authors declare no conflict of interest.

Data Availability Statement

The data that support the findings of this study are available from the corresponding author upon reasonable request.

Keywords: chemical bonding · heterolytic scissions · homolytic scissions · density functional theory · nitrile imine

[1] L. Ortiz-Rojano, J. Rojas-Martín, C. Rodríguez-Diaz, M. C. Carreño, M. Ribagorda, *Chem. A Eur. J.* **2019**, *25*, 15050.
[2] J. Deng, X. Wu, G. Guo, X. Zhao, Z. Yu, *Org. Biomol. Chem.* **2020**, *18*, 5602.
[3] Y. He, D. H. Xu, Y. J. Zhang, C. Zhang, J. M. Guo, L. Li, X. Q. Liang, *RSC Adv.* **2021**, *11*, 32792.
[4] Y. Sugawara, N. Jasinski, M. Kaupp, A. Welle, N. Zydziak, E. Blasco, C. Barner-Kowollik, *Chem. Commun.* **2015**, *51*, 13000.
[5] E. Blasco, Y. Sugawara, P. Lederhose, J. P. Blinco, A. M. Kelterer, C. Barner-Kowollik, *ChemPhotoChem* **2017**, *1*, 159.
[6] S. Flesch, P. Vöhringer, *Angew. Chem.* **2022**, *134*, e202205803.
[7] C. Jamieson, K. Livingstone, *The Nitrile Imine 1,3-Dipole: Properties, Reactivity and Applications*, Springer International Publishing, **2020**.
[8] H. M. Muchall, *J. Phys. Chem. A* **2011**, *115*, 13694.
[9] M. M. Montero-Campillo, I. Alkorta, J. Elguero, *Sci. Reports* **2017**, *7*, 6115.
[10] G. Bertrand, C. Wentrup, *Angew. Chem. Int. Ed. Engl.* **1994**, *33*, 527.
[11] K. Bhattacharyya, D. Ramaiah, P. K. Das, M. V. George, *J. Photochem.* **1987**, *36*, 63.
[12] D. Bégué, G. G. Qiao, C. Wentrup, *J. Am. Chem. Soc.* **2012**, *134*, 5339.
[13] D. Bégué, C. Wentrup, *J. Org. Chem.* **2014**, *79*, 1418.
[14] N. H. Toubro, A. Holm, *J. Am. Chem. Soc.* **1980**, *102*, 2093.
[15] K. Ishida, K. Morokuma, A. Komornicki, *J. Chem. Phys.* **2008**, *66*, 2153.
[16] S. Maeda, Y. Harabuchi, Y. Ono, T. Taketsugu, K. Morokuma, *Int. J. Quantum Chem.* **2015**, *115*, 258.
[17] E. Matito, B. Silvi, M. Duran, M. Solà, *J. Chem. Phys.* **2006**, *125*, 024301.
[18] A. D. Becke, K. E. Edgecombe, *J. Chem. Phys.* **1990**, *92*, 5397.
[19] A. Savin, B. Silvi, F. Colonna, *Can. J. Chem.* **1996**, *74*, 1088.

[20] B. Silvi, A. Savin, *Nature* **1994**, *371*, 683.
[21] A. Savin, R. Nesper, S. Wengert, T. F. Fässler, *Angew. Chem. Int. Ed.* **1997**, *36*, 1808.
[22] J. Andrés, S. Berski, B. Silvi, *Chem. Commun.* **2016**, *52*, 8183.
[23] J. Contreras-García, J. M. Recio, *J. Phys. Chem. C* **2011**, *115*, 257.
[24] C. Gatti, *Zeitschrift fur Krist.* **2005**, *220*, 399.
[25] V. Tsirelson, A. Stash, *Chem. Phys. Lett.* **2002**, *351*, 142.
[26] X. Krokidis, S. Noury, B. Silvi, *J. Phys. Chem. A* **1997**, *101*, 7277.
[27] L. Ayarde-Henríquez, C. Guerra, M. Duque-Noreña, E. Rincón, P. Pérez, E. Chamorro, *J. Phys. Chem. A* **2021**, *125*, 5152.
[28] C. Guerra, L. Ayarde-Henríquez, M. Duque-Noreña, C. Cárdenas, P. Pérez, E. Chamorro, *Phys. Chem. Chem. Phys.* **2021**, *23*, 20598.
[29] L. R. Domingo, *RSC Adv.* **2014**, *4*, 32415.
[30] E. Chamorro, M. Duque-Noreña, N. Gutierrez-Sánchez, E. Rincón, L. R. Domingo, *J. Org. Chem.* **2020**, *85*.
[31] J. Andrés, S. Berski, L. R. Domingo, P. González-Navarrete, *J. Comput. Chem.* **2012**, *33*, 748.
[32] B. Silvi, R. J. Gillespie, *The ELF Topological Analysis Contribution to Conceptual Chemistry and Phenomenological Models*, **2007**.
[33] E. Taxil, L. Bagnol, J. H. Horner, M. Newcomb, *Org. Lett.* **2003**, *5*, 827.
[34] P. O. Whitted, J. H. Horner, M. Newcomb, X. Huang, D. Crich, *Org. Lett.* **1999**, *1*, 153.
[35] P. Wan, S. Muralidharan, *J. Am. Chem. Soc.* **1988**, *110*, 4336.
[36] O. Lanzalunga, A. Lapi, *J. Sulfur Chem.* **2012**, *33*, 101.
[37] F. Feixas, E. Matito, M. Duran, M. Solà, B. Silvi, *J. Chem. Theory Comput.* **2010**, *6*, 2736.
[38] S. Noury, X. Krokidis, F. Fuster, B. Silvi, *Comput. Chem.* **1999**, *23*, 597.
[39] T. Lu, F. Chen, *J. Comput. Chem.* **2012**, *33*, 580.
[40] A. D. Becke, *Int. J. Quantum Chem.* **1983**, *23*, 1915.
[41] B. Silvi, *J. Mol. Struct.* **2002**, *614*, 3.
[42] J. Andrés, P. González-Navarrete, V. S. Safont, *Int. J. Quantum Chem.* **2014**, *114*, 1239.
[43] V. Polo, J. Andrés, *J. Comput. Chem.* **2005**, *26*, 1427.

Manuscript received: November 21, 2022
Revised manuscript received: March 5, 2023
Version of record online: March 23, 2023